AIAA JOURNAL
Vol. 36, No. 3, March 1998

Failure of Adhesive-Bonded Composite Single Lap Joints with Embedded Cracks

L. Tong*
University of Sydney, Sydney, New South Wales 2006, Australia

An experimental and analytical study is presented to investigate the effect of cracks embedded in continuous adherends near overlap ends on failure behavior of adhesive-bonded composite single lap joints. In the experimental part, the effects of the crack size and location on both failure loads and failure modes are illustrated. A nonlinear finite element analysis (FEA) is presented to demonstrate the effect of the cracks on the stress distribution in the adhesive layer. Based on the FEA results, an analytical model is developed to study the effect of the cracks on the strengths of the joints. The energy release rates of modes I and II are calculated using both FEA and the present analytical model. Two failure criteria, one based on the critical energy release rate and the other based on the maximum stress, are used to predict the failure loads of the specimens. It is shown that there is a good correlation between the average measured failure loads and those predicted using FEA and the analytical models with the maximum-stress-based criterion. Based on the present results, it is concluded that short cracks at the chosen locations can cause larger reduction in the failure loads of adhesive-bonded single lap joints than long cracks.

I. Introduction

INTERLAMINAR or intraply delamination is a typical failure mode observed in an adhesive-bonded composite single lap joint.[1,2] The two major contributing factors are considered to be the high gradient of peel stress at overlap ends and the interlaminar weakness of composite adherends. Although a lot of work has been done to understand and predict failure behavior of adhesive-bonded single lap joints,[1,3–7] there has been little effort devoted to investigating the effect of cracks embedded in continuous adherends on failure mechanism of adhesive-bonded lap joints. Investigation of these effects not only can provide us with an alternative method for predicting joint strength but also can be used as a basis for investigation of damage tolerance of adhesive-bonded composite lap joints.

The objective of this study is to investigate the effects of embedded cracks on the stress distributions in adhesive layer, the stresses in adherends, and the failure loads of adhesive-bonded composite single lap joints. In doing so, this study considers an adhesive-bonded composite single lap joint, as shown schematically in Fig. 1, subjected to an axial load P. The joint is assumed to be a balanced one in which the two adherends have the same layup and free length l. The adherend thickness is t, and the overlap length is $2c$. The two cracks are assumed to be located in the continuous adherends near overlap ends, and they are of the same length a and located at equal distance $0.5d$ from the midpoint of the overlap and at same distance beneath the surface ply adjacent to the adhesive layer. In the following sections, experimental results are presented first to show the effects of crack size and location on the failure loads and modes. A nonlinear finite element analysis (FEA) is presented to show the effect of crack size on the stress distribution in the adhesive layer. An analytical model is developed and then validated against the FEA results. The effect of crack size on the energy release rates at crack tips is also illustrated using both FEA and analytical analysis results.

II. Experimental Investigation

A. Specimen and Testing Procedure

The specimens used in this study were adhesive-bonded composite single lap joints as shown in Fig. 1. The material used was T300/934 carbon/epoxy plain woven prepreg manufactured by Fiberite Corporation by impregnating the Fiberite 934 epoxy resin on T300 plain woven fabrics (supplier product designation was HMF-5-322/34C). The prepreg has a fiber tow size of 3000 filaments per tow and a 177°C curing temperature and possesses the same mechanical properties in both warp and weft directions. Composite panels of 250 × 250 mm were manufactured by laminating eight plies of T300/934 plain woven prepreg in 0-deg direction, i.e., $(0)_{8S}$. Each ply had a nominal thickness of 0.215 mm. During the layup process, two plies of 0.02-mm-thick Teflon® film of different widths were embedded between the surface and second ply to model cracks of different lengths at the chosen locations. Although the use of Teflon film to model cracks is a common practice, it can be argued that such a practice tends to form a notch rather than a sharp crack. All panels were then cured in an autoclave following the manufacturer's recommended curing cycle.[8] After curing, all panels were cut carefully to ensure that all of the Teflon films stayed at the right position. Following a moderate hand sanding with sandpaper and an acetone wash, two panels were bonded together using FM300-K film adhesives from Cytec in an autoclave following the manufacturer's recommended curing cycles. Metal shims were used to achieve a uniform bondline thickness of 0.16 mm. Positioning holes and fasteners were used to ensure minimum relative in-plane movement during bonding and, thus, to achieve the desired relative distance d (see Fig. 1). Specimens of 25.4 mm width were prepared by cutting the panels in such a way that there were no metal shims left in the bonding area. Aluminum end taps of 25.4 × 40 mm were bonded using an instant adhesive applied to both ends of the adherends to overcome the eccentricity introduced when installing a specimen on the testing machine.

Six specimen configurations were considered, and they are referred to as specimen groups A–F, respectively. There were five specimens in groups B–E, and groups A and F had only three and four specimens. As defined in Fig. 1, for all specimens the unsupported length l was 100 mm, the overlap length $2c$ was 50 mm, the specimen width was 25.4 mm, and the adherend thickness t was 1.72 mm. In addition, the two cracks were embedded between the first and second plies 0.215 mm beneath the surface, i.e., $t_1 = 0.215$ mm. Other parameters defining the location and size of the embedded cracks in all specimens are given in Table 1. There was no crack embedded in specimen group A. Specimens in groups B, C, and D had two cracks of 4, 6, and 8 mm length, respectively, with an offset distance d of 50 mm between the two crack centers. Specimens in group E had both cracks of 6 mm length embedded outside the joint overlap ($d = 60$ mm), whereas specimens in group F had both cracks of 6 mm length located inside the joint overlap ($d = 40$ mm).

All specimens were loaded in axial tension on an Instron testing machine at room temperature. A loading rate of 0.5 mm/min was used for all specimens. The applied load and the crosshead displacement were recorded.

Received June 14, 1997; revision received Oct. 29, 1997; accepted for publication Nov. 4, 1997. Copyright © 1997 by the American Institute of Aeronautics and Astronautics, Inc. All rights reserved.

*Senior Lecturer, Department of Aeronautical Engineering.

Table 1 Dimensions of single lap joints with cracks

Specimen group	Offset distance d, mm	Crack length a, mm
A	50	0
B	50	4
C	50	6
D	50	8
E	60	6
F	40	6

Table 2 Failure loads and modes of specimen group A

Specimen	Failure load, N	Failure mode, mm
A2	14,374	a (6)
A3	14,064	a (6–7)
A4	14,076	a (5–6)
Average	14,171	——

Table 3 Failure loads and modes of specimen group B

Specimen	Failure load, N	Failure mode, mm
B1	12,215	——[a]
B2	12,273	b (0)
B3	12,663	b (2)
B4	13,628	b (4)
B5	12,209	b (3)
Average	12,598	——

[a] Intraply or interlaminar delamination in one surface ply in the full length of the overlap.

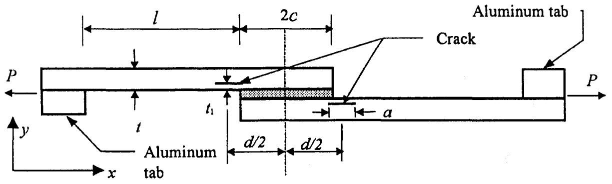

Fig. 1 Typical single lap joint with two embedded cracks.

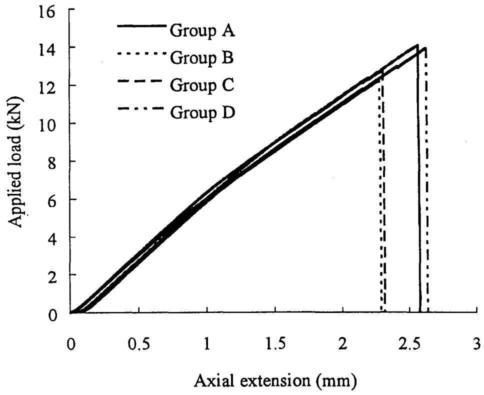

Fig. 2 Typical curves of the applied load vs the crosshead displacement.

B. Results and Discussion

The measured axial loads increased almost linearly with the crosshead displacement for all specimens up to the ultimate fracture loads accompanied by a bang. However, micro-cracking was audible at lower load levels prior to final fracture of the specimens. Typical load-displacement curves are shown in Fig. 2. It is noted that the embedded cracks only cause a slight change in the overall stiffness of the specimens.

Table 4 Failure loads and modes of specimen group C

Specimen	Failure load, N	Failure mode, mm
C1	14,216	b[a]
C2	12,280	b (2–3)
C3	12,885	b (2–3)
C4	12,929	b (3–4)
C5	12,709	b (2–3)
Average	13,004	——

[a] Failure mode b denoted by dotted lines; see Fig. 3b.

Table 5 Failure loads and modes of specimen group D

Specimen	Failure load, N	Failure mode, mm
D1	13,051	b (2–3)
D2	13,168	b (2–5)
D3	12,667	b (0–1)
D4	14,172	b[a]
D5	13,916	b (2–3)
Average	13,395	——

[a] Failure mode b denoted by dotted lines; see Fig. 3b.

Table 6 Failure loads and modes of specimen group E

Specimen	Failure load, N	Failure mode, mm
E1	13,241	a[a]
E2	14,852	a (0–2)
E3	14,948	a (2–3)
E4	14,247	a (0–2)
E5	12,812	a[a]
Average	14,020	——

[a] Failure mode a denoted by dotted lines; see Fig. 3a.

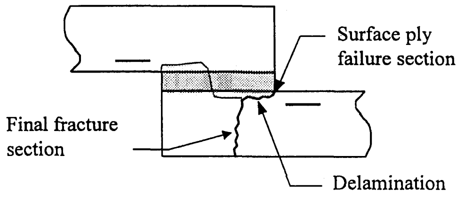

a) Specimen groups A and E

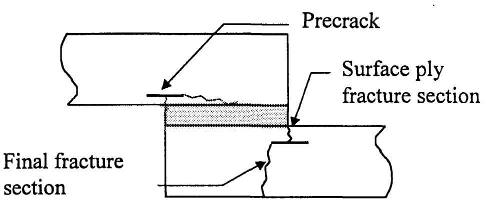

b) Specimen groups B, C, and D

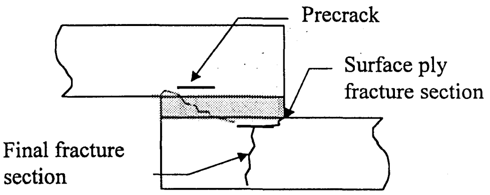

c) Specimen group F

Fig. 3 Typical fracture modes (solid curves indicate typical cracks and dotted lines indicate cracks for one or two specimens in the group).

Tables 2–7 summarize the ultimate failure loads and the associated failure modes. Inspection of the average measured failure loads in Tables 2–5 reveals that the average failure loads of specimen groups B, C, and D are 11.1, 9.2, and 5.5% lower than that of specimen group A. This result clearly indicates that 1) the embedded cracks in specimen groups B, C, and D can cause a noticeable reduction in the failure load and that 2) short cracks cause larger reduction in failure load than long cracks when the crack centers are placed right at the overlap ends. From this observation, it can be said that the adhesive-bonded single lap joints tend to be tolerant to long cracks and to be less tolerant to short cracks. One reason for this is that the crack tip in the overlap is subjected to high peel and shear stresses when it nears the overlap end. The average failure load of specimen group F in Table 7 shows that the cracks embedded in the overlap can reduce the average failure load by 6.4% compared to that of specimen group A. This 6.4% reduction in failure load is smaller than the 9.2% of group C, and this indicates that moving the cracks away from the high peel and shear stresses zone near the overlap end can lessen the effect of the embedded cracks in terms of reducing the failure load. Finally, by comparing the average failure loads of specimen groups A and E (see Tables 2 and 6), it is noted that the embedded cracks do not seem to affect the ultimate failure load. This observation indicates that the joints are not sensitive to the embedded cracks located outside the joint overlap.

Inspection of the failure surfaces of all specimens revealed that there were three typical failure modes. These three types of failure modes are referred as to failure modes a, b, and c, respectively, in the third columns of Tables 2–7 and are schematically shown in Fig. 3 from their side views. For each half-overlap of nearly all specimens, there exists a surface ply fracture section and a final complete fracture of the remaining section. These two fracture sections were observed to be linked via an interlaminar delamination for most cracked joints or an intraply delamination for most virgin-type joints, as clearly shown in Fig. 4. The delamination length between the two fractured sections is listed by the numbers in parentheses in the third columns of Tables 2–7. The range of the delamination length indicates a nonuniform final complete sectional fracture and, thus, implies a nonuniform crack propagation at the crack tips inside the overlap. A detailed discussion of these failure modes for each specimen configuration follows.

Table 7 Failure loads and modes of specimen group F

Specimen	Failure load, N	Failure mode, mm
F1	13,773	c (4–6)
F3	13,169	c (5–6)
F4	12,924	c (5–6)
F5	13,186	c (4–5)
Average	13,263	——

1. *Failure Mode a (see Fig. 3a)*

Initial sectional fracture due to high tensile stress in the surface ply developed into an intraply or interlaminar delamination and then

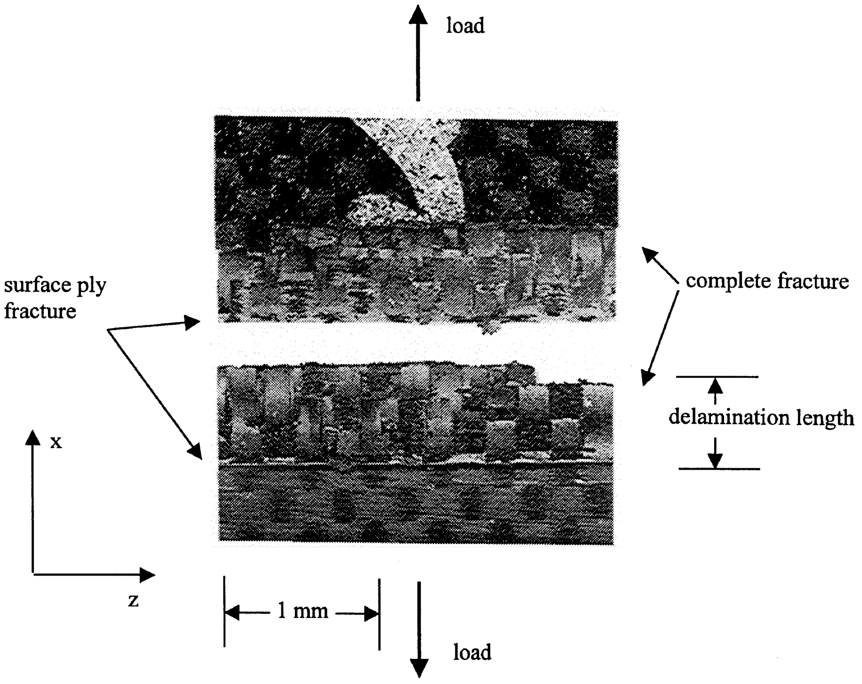

a) Specimen group A

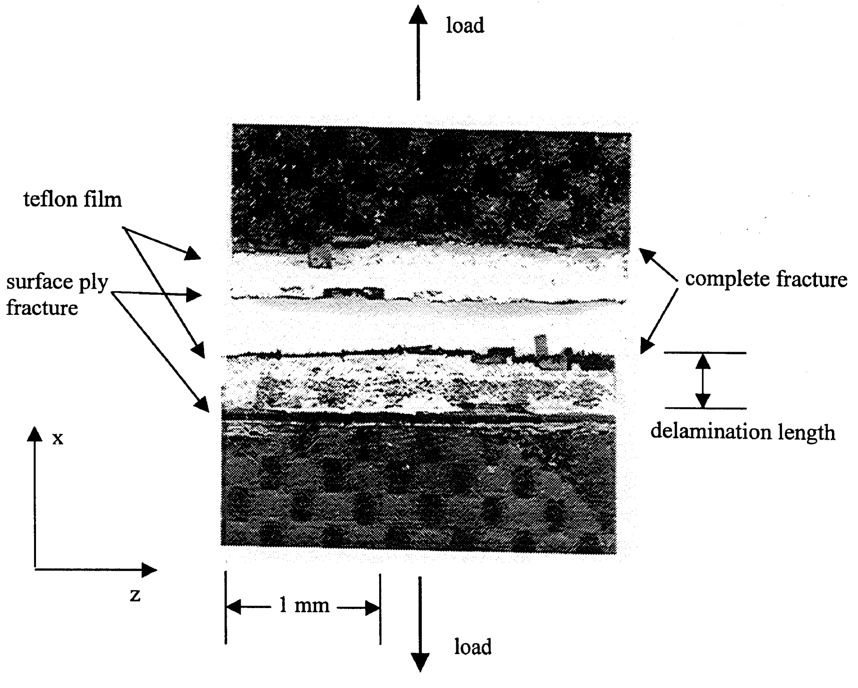

b) Specimen group B

Fig. 4 Photographs of typical failure surfaces.

led to the final fracture of the remaining cross section. All virgin-type specimens in group A exhibited failure in failure mode a. As can be seen in Fig. 4a, the delamination was not uniform across the specimen width and its length ranged from 5 to 7 mm as given by the numbers in parentheses in the third column of Table 2. Most specimens in group E also failed in failure mode a with nonuniform delamination varying from 0 to 3 mm (see Table 6), except for two specimens that exhibited a failure mode as shown schematically by the dotted line in Fig. 3a.

2. *Failure Mode b (see Fig. 3b)*

Initial sectional breakage occurred in the surface ply and then resulted in a final net sectional fracture near the crack tip in the overlap. This was a typical failure mode for most specimens in groups B, C, and D as shown by the solid lines in Figs. 3b and 4b. The final net fracture sections were not uniform and measured from 0 to 5 mm away from the initial fracture section (detailed numbers for each specimen are given in parentheses in the third columns of Tables 3–5). However, there were two specimens for which sectional breakage also took place in the surface ply at the other end of the overlap and developed into an intraply or interlaminar delamination toward the center of the overlap, as shown by the dotted lines in Fig. 3b.

3. *Failure Mode c (see Fig. 3c)*

Sectional fracture occurred in the surface ply at an overlap end and then developed into an interlaminar or intraply delamination that connected to the embedded crack near the crack tip. The final net sectional fracture occurred at about half of the embedded crack length or 4–6 mm away from the overlap end as given in the third column of Table 7. This is the typical failure mode for most specimens in specimen group F, except for one specimen in which fracture took place as shown by the dotted line in Fig. 3c.

III. FEA Model

A two-dimensional plane strain FEA procedure was used to model the behavior of adhesive-bonded single lap joint specimens with and without cracks using Strand6.[9] Geometrical nonlinearity was included in the analyses to account for large rotation and deflection that occurred in the overlap. All dimensions for each specimen configuration have been given in detail in the preceding section. The mechanical properties for a T300/934 cloth ply are given in Table 8 (Refs. 8 and 10). The in-plane tensile strength is 518 MPa, which was measured following the American Society for Testing and Materials standard. The critical energy release rates of modes I and II for the T300/934 plain weave material are $G_{IC} = 0.23\,\mathrm{kJ/m^2}$ and $G_{IIC} = 0.66\,\mathrm{kJ/m^2}$ (Ref. 11). Table 9 tabulates Young's modulus and Poisson's ratio for FM300K film adhesive.

Four-node quadrilateral plane strain elements were used to model the adherends and the bondline. Two meshing schemes were used to test mesh dependency. In the first meshing scheme, one element was used for each ply and the bondline in the through-the-thickness direction. A fine mesh with elements of 0.2121 mm length was adopted near overlap ends and cracks tips, and a coarse mesh with elements of up to 1 mm length was used in the remaining areas. In the second meshing scheme, a 3 × 3 division was used to subdivide the nearly square elements near the crack tips and the overlap ends. These subdivided elements include the four elements near each crack tip and the four elements on both sides of each overlap end. Three elements were used for the surface and second ply between the crack tips. Small rectangular elements (0.0707 × 0.0667 mm) were used in the vicinities of the crack tips, as shown in Fig. 5. Finite element models were generated to model all specimen configurations. In addition, an FEA model was generated to simulate a joint configuration with two 2-mm-long cracks. This model is referred to as configuration G for the sake of convenience.

The single lap joint modeled in Fig. 5 was loaded with an applied axial load P. Both ends of the joint were modeled as being fully clamped. Numerical results were obtained using both meshing schemes for the five adhesive-bonded single lap joints with and without cracks when subjected to an axial load $P = 590$ N/mm. Geometrical nonlinearity was considered, and 20 load increments were used to apply the load. Figures 6 and 7 show the distribution of the shear stress σ_{xy} and normal stress σ_{yy} in the adhesive layer obtained using the second meshing scheme. For the joints with cracks, the cracks are 2, 4, 6, and 8 mm long and are located between the first and second ply beneath the surface. Figures 6 and 7 show that the shear stress σ_{xy} and normal stress σ_{yy} in the adhesive layer in a joint with embedded cracks are different from those without a crack. Figure 6 reveals that, compared to the shear stress of an uncracked joint, the shear stress in the adhesive layer of a cracked joint is smaller between the overlap end and the crack tip and is larger between the overlap center and a point slightly away from the crack tip. Figure 7 shows that the peak peel stress is reduced due to presence of the cracks, and this reduction is accompanied by the appearance of another small peak peel stress.

Table 8 Mechanical properties of a cloth ply (nominal ply thickness, 0.215 mm)

Longitudinal modulus $E_1 = E_2$, MPa	57,226
Transverse modulus E_3, MPa	4,800
In-plane shear modulus G_{12}, MPa	4,481
Out-of-plane shear modulus $G_{13} = G_{23}$, MPa	4,400
In-plane Poisson ratio μ_{12}	0.05
Out-of-plane Poisson ratio $\mu_{13} = \mu_{23}$	0.28

Table 9 Mechanical properties of FM300K film adhesive (nominal bondline thickness 0.16 mm)

Young's modulus E, MPa	2400
Poisson ratio μ	0.32

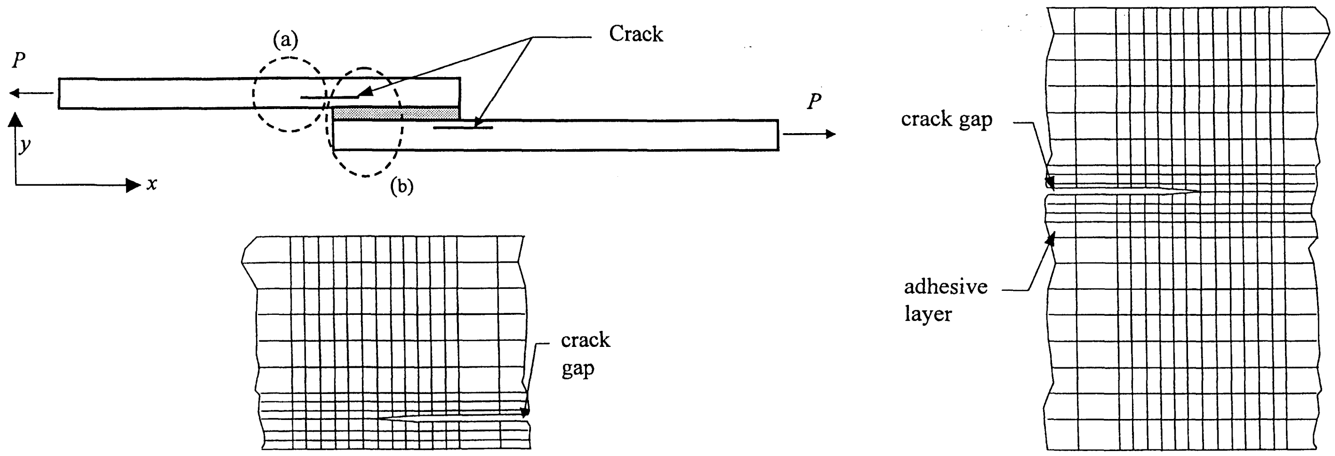

a) Mesh used near crack tip B

b) Mesh used near crack tip A

Fig. 5 Meshes used near the crack tips.

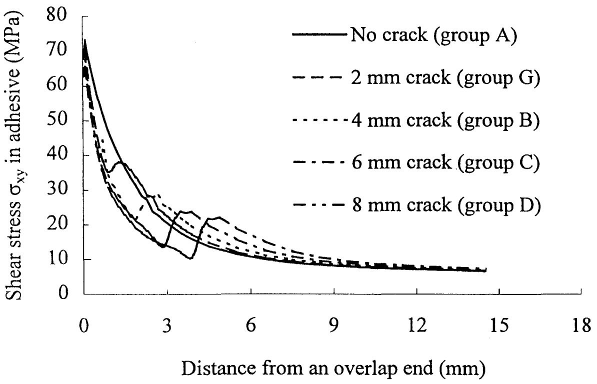

Fig. 6 Effect of crack size on the shear stress distribution.

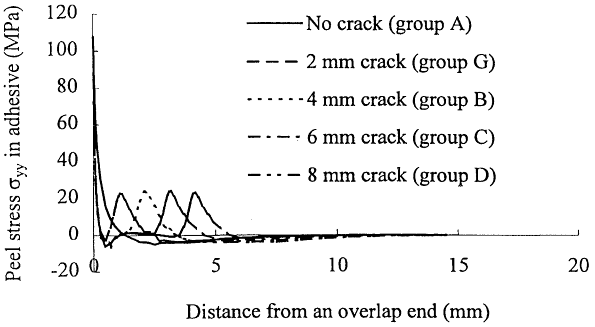

Fig. 7 Effect of crack size on the peel stress distribution.

Numerical results also show that singularities exist at both ends of the overlap and the four crack tips because only purely elastic analysis was conducted. Comparison of the two meshing schemes indicates that the calculated stresses in the vicinities of the overlap ends and the crack tips seem to be mesh dependent. Note that singularities and mesh dependence exist even though an elastic–plastic analysis was carried out.[12] However, based on the results of the models developed using both meshing schemes, the calculated stresses at crack tip A within the overlap are larger than those at crack tip B outside the overlap. This correlates well to the experimentally observed failure mechanism that cracks propagated at crack tip A. However, this needs to be confirmed by energy release rates at crack tips A and B, to be discussed later.

IV. Analytical Model

When a crack is located between two adjacent plies in an adherend (see Fig. 1), the existence of this crack significantly redistributes the stresses in the adhesive layer (see Figs. 6 and 7) and, thus, changes the stress resultants in both adherends. This makes an analytical analysis more difficult and challenging. A simple analytical model will be developed to calculate the energy release rates at the crack tips in terms of the stress resultants in different parts of the adherends determined using a global and a local analysis. The peel and shear stresses in the adhesive layer will not be included in the global analysis.

Because of symmetry, we consider only one crack as shown in Fig. 8. The crack has a crack tip at section A inside the overlap and a crack tip at section B outside the joint overlap. As shown in Fig. 9, the crack has a length of $X_A + X_B$, where X_A is the length of the crack part inside the overlap and X_B is the length of the crack part outside the overlap. In Fig. 9a, at crack tip A both the adherends and adhesive layer are modeled as a beam with an embedded crack that is located at a distance of $t - t_1$ from the top surface. In Fig. 9b, at crack tip B the adherend is modeled as a beam with a crack located at a distance of t_1 from the lower surface of the adherend. The analysis procedure for the present model will consist of 1) a global analysis of the joints, 2) a local analysis of the cracked portion of the joints, and 3) calculation of energy release rates at the crack tips.

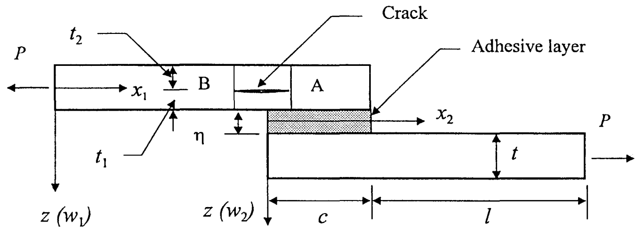

Fig. 8 Adhesive-bonded composite single lap joint with an embedded crack.

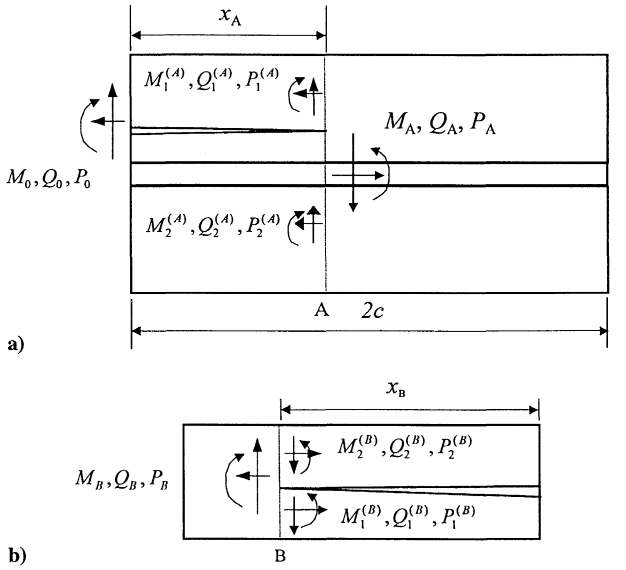

Fig. 9 Stress resultants acting on the cross sections of crack tips A and B.

A. Global Analysis

The global analysis aims to determine the bending moments, transverse shear forces, longitudinal forces, and the transverse deflections, as well as their slopes at crack tips A and B. To do this, it is assumed that presence of the two cracks does not significantly change the stress resultants and the deflections at crack tips A and B. The solution presented by Goland and Reissner[3] for an adhesive-bonded single lap joint will be rewritten for our global analysis of an adhesive-bonded composite single lap joint as follows:

$$w_1 = -\frac{kt}{2}\frac{\sinh u_1 x_1}{\sinh u_1 l} + \alpha_n x_1, \qquad 0 \le x_1 \le l \qquad (1)$$

$$w_2 = \frac{(1-k)t}{2}\cosh u_2 x_2 - \frac{kt}{2}\frac{u_1}{u_2}\frac{\cosh u_1 l}{\sinh u_1 l}\sinh u_2 x_2 + \alpha_n (l + x_2) - \frac{t}{2}, \qquad 0 \le x_2 \le c \qquad (2)$$

where w_1 and w_2 are the transverse deflections of the unsupported adherend and the overlap part, respectively, as shown in Fig. 8. Also,

$$\alpha_n = \frac{t}{2(l+c)}$$

$$k = \frac{\cosh u_2 c \sinh u_1 l}{\cosh u_2 c \sinh u_1 l + (u_1/u_2)\sinh u_2 c \cosh u_1 l} \qquad (3)$$

$$u_i = \sqrt{\frac{P}{D_i}} \quad (i = 1, 2), \qquad D_1 = \frac{Q_{11} t^3}{12}$$

$$D_2 = 8D_1, \qquad Q_{11} = \frac{E_1}{1 - \nu_{12}\nu_{21}}$$

where α_n and k are the eccentric coefficient and the bending moment factor, respectively. D_1 and D_2 are the adherend bending stiffness

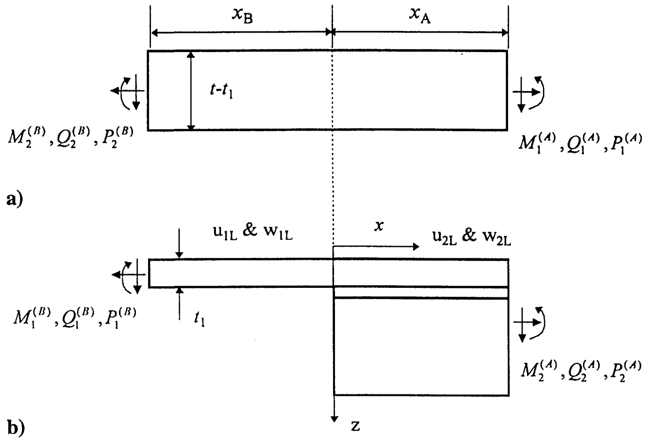

Fig. 10 Free body diagram for the upper and lower parts of the cracked segment of the joint between crack tips A and B.

and the overall bending stiffness of the overlap part. E_1 is Young's modulus of a composite ply in the fiber direction, and ν_{12} and ν_{21} are the major and minor Poisson's ratios.

The global bending moments M_A and M_B and the shear forces Q_A and Q_B can be obtained using the following two classical equations:

$$M_B = \frac{kPt}{2}\frac{\sinh u_1(l-x_B)}{\sinh u_1 l}, \qquad Q_B = \frac{kPtu_1}{2}\frac{\cosh u_1(l-x_B)}{\sinh u_1 l} \tag{4}$$

$$M_A = \frac{Pt}{2}\cosh u_2 x_A\left[-1+k\left(1+\frac{u_1}{u_2}\frac{\tanh u_2 x_A}{\tanh u_1 l}\right)\right] \tag{5}$$

$$Q_A = \frac{Pt}{2}u_2\sinh u_2 x_A\left[-1+k\left(1+\frac{u_1}{u_2}\frac{1}{\tanh u_1 l}\frac{1}{\tanh u_2 x_A}\right)\right]$$

B. Local Analysis

The cracked portion of the joint can be divided into two free bodies as shown in Figs. 10a and 10b. In Fig. 10b, the free body is a beam having different cross sections. A new x–z coordinate system is introduced for the beam shown in Fig. 10b, in which x is measured from the overlap end and in the direction of the overlap center, whereas z is measured from the midplane of the left and right parts of the beam. The coordinate x ranges from $-x_B$ to 0 for the left part and from 0 to x_A for the right part. The axial and lateral displacements in the left and right parts of the lower beam are u_{1L} and w_{1L} and u_{2L} and w_{2L}, respectively. The axial force, bending moment, and transverse shear force will be determined based on the assumption that the lower part satisfies all of the continuity conditions at the cross sections of both crack tips A and B.

1. Axial Forces at Cross Sections A and B

Consider the lower part of the cracked joint as shown in Fig. 10b; the governing equations for axial deformation are given by

$$\frac{\mathrm{d}N_{iL}}{\mathrm{d}x} = 0, \qquad N_{iL} = A_{iL}\varepsilon_{iL}, \qquad \varepsilon_{iL} = \frac{\mathrm{d}u_{iL}}{\mathrm{d}x} \qquad (i = 1, 2) \tag{6}$$

where N_{iL}, ε_{iL}, and u_{iL} are the axial forces, the strains, and the axial displacements, respectively, and $A_{1L} = Q_{11}t_1$ and $A_{1L} = Q_{11}(t + t_1)$. The boundary conditions at both ends of the lower beam are

$$\begin{aligned} u_{1L} &= u_B - \frac{t-t_1}{2}\left.\frac{\mathrm{d}w_1}{\mathrm{d}x_1}\right|_{x_1=l-x_B} && (\text{at}\, x = -x_B) \\ u_{2L} &= u_A - \frac{t-\eta-t_1}{2}\left.\frac{\mathrm{d}w_2}{\mathrm{d}x_2}\right|_{x_2=x_A} && (\text{at}\, x = x_A) \end{aligned} \tag{7}$$

where u_A and u_B are the global axial displacements at points A and B, respectively, and can be determined in terms of the applied load P and the axial stiffness of the joint. The continuity conditions at $x = 0$ are

$$u_{1L} = u_{2L}, \qquad N_{1L} = N_{2L} \tag{8}$$

By solving Eqs. (6–8), we can determine the axial displacement u_1 and u_2. Then we can find the axial force at end B of the beam as follows:

$$P_1^{(B)} = \frac{Q_{11}t_1}{x_A + [t_1/(t+t_1)]x_B} \times\left[\frac{P}{Q_{11}t}\left(\frac{x_A}{2}+x_B\right)+\frac{t-t_1}{2}\left.\frac{\mathrm{d}w_1}{\mathrm{d}x_1}\right|_{x_1=l-x_B} - \frac{t-t_1}{2}\left.\frac{\mathrm{d}w_2}{\mathrm{d}x_2}\right|_{x_2=x_A}\right] \tag{9}$$

Using the equilibrium conditions of the two free beams, we can determine the axial forces at both ends of the lower beam:

$$P_2^{(A)} = P_1^{(B)}, \qquad P_2^{(B)} = P - P_1^{(B)}, \qquad P_1^{(A)} = P - P_2^{(A)} \tag{10}$$

2. Bending Moments and Shear Forces at Cross Sections A and B

Consider the lower part of the cracked joint as shown in Fig. 10b; the governing equations for bending deformation are given by

$$\begin{gathered} \frac{\mathrm{d}Q_{iL}}{\mathrm{d}x} = 0, \qquad Q_{iL} = \frac{\mathrm{d}M_{iL}}{\mathrm{d}x} \\ M_{iL} = -D_{iL}\kappa_{iL}, \qquad \kappa_{iL} = \frac{\mathrm{d}^2 w_{iL}}{\mathrm{d}x^2} \qquad (i = 1, 2) \end{gathered} \tag{11}$$

where Q_{iL}, M_{iL}, κ_{iL}, and w_{iL} are the shear forces, bending moments, bending curvatures, and lateral displacements, respectively, and $D_{1L} = Q_{11}t_1^3/12$ and $D_{2L} = Q_{11}(t + t_1)^3/12$. The boundary conditions at both ends of the lower beam are

$$\begin{aligned} w_{1L} &= w_1|_{x_1=l-x_B}, & \frac{\mathrm{d}w_{1L}}{\mathrm{d}x} &= \left.\frac{\mathrm{d}w_1}{\mathrm{d}x_1}\right|_{x_1=l-x_B} && (\text{at}\, x = -x_B) \\ w_{2L} &= w_2|_{x_2=x_A}, & \frac{\mathrm{d}w_{2L}}{\mathrm{d}x} &= \left.\frac{\mathrm{d}w_2}{\mathrm{d}x_2}\right|_{x_2=x_A} && (\text{at}\, x = x_A) \end{aligned} \tag{12}$$

where w_1 and w_2 are the global lateral displacements as given in Eqs. (1) and (2). The continuity conditions at $x = 0$ are

$$\begin{gathered} w_{1L} = w_{2L}, \qquad \frac{\mathrm{d}w_{1L}}{\mathrm{d}x} = \frac{\mathrm{d}w_{2L}}{\mathrm{d}x} \\ M_{1L} = M_{2L} + 0.5tP_1^{(B)}, \qquad Q_{1L} = Q_{2L} \end{gathered} \tag{13}$$

By solving Eqs. (11–13), we can determine the lateral displacements w_1 and w_2

$$\begin{gathered} w_1 = c_0 + c_1 x + \tfrac{1}{2}c_2 x^2 + \tfrac{1}{6}c_3 x^3 \\ w_1 = c_4 + c_5 x + \tfrac{1}{2}c_6 x^2 + \tfrac{1}{6}c_7 x^3 \end{gathered} \tag{14}$$

where c_i are constants and are given in the Appendix. Using the lateral displacements and Eqs. (11), we can find the bending moments and the shear forces at cracks A and B, namely, $M_i^{(B)}$, $Q_i^{(B)}$, $M_i^{(A)}$, and $Q_i^{(A)} (i = 1, 2)$, as shown in Fig. 10.

C. Numerical Results and Discussion

To validate the present analytical model, let us consider the four cracked single lap joints that have been analyzed using the finite element method based on the second meshing scheme. These four joints are the three specimen configurations in specimen groups B, C, and D with a crack length of 4, 6, and 8 mm, respectively, and a joint referred to as configuration G having a crack length of 2 mm. The applied load is 590 N/mm, the same as that used for the FEA.

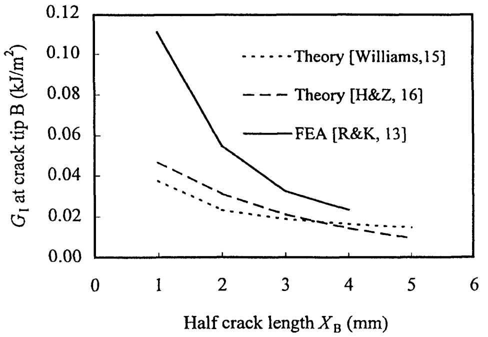

Fig. 11a Mode I energy release rate at crack tip B vs the half-crack length x_B.

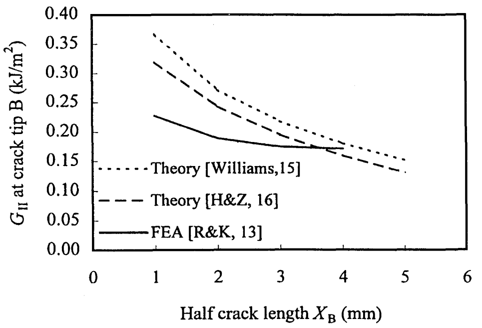

Fig. 11b Mode II energy release rate at crack tip B vs the half-crack length x_B.

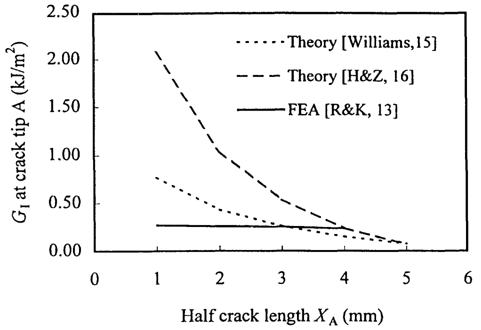

Fig. 11c Mode I energy release rate at crack tip A vs the half-crack length x_A.

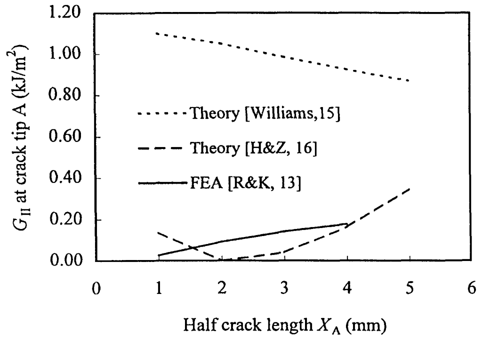

Fig. 11d Mode II energy release rate at crack tip A vs the half-crack length x_A.

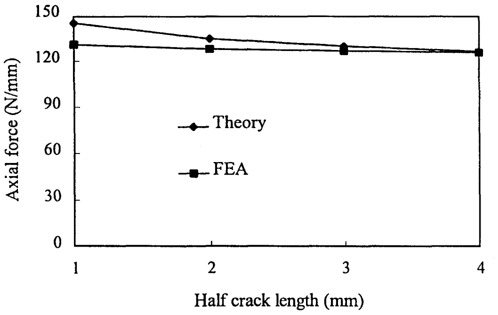

Fig. 12 Axial force $P_1^{(B)}$ predicted using FEA and analytical model vs the half-crack length x_A.

Figures 11a–11d show the energy release rates of modes I and II at crack tips B and A calculated using the FEA and the present analytical model. In the FEA, the modified crack closure integral method was used to calculate the mode I and mode II energy release rates.[13,14] In the analysis, the equations given by Williams[15] and Hutchinson and Suo[16] were employed by inputting the present axial forces, shear forces, and bending moments at crack tip A (Fig. 9a) and crack tip B (Fig. 9b).

Figures 11a and 11b show that the mode I and mode II energy release rates at crack tip B decrease as the crack becomes longer; that is, the smaller the half-crack length x_B, the larger the energy release rates. This indicates that crack propagation will initiate at a lower load for joints with a small x_B and at a higher load for joints with a large x_B. It is noted that the analytical models tend to predict a lower mode I energy release rate and a higher mode II energy release rate compared to those results calculated by FEA. However, a reasonably good correlation is observed among the energy release rates when x_B is larger than 3 mm.

Figure 11c plots the mode I energy release rate at crack tip A vs the half-crack length x_A. All models predict that the mode I energy release rate at crack tip A decreases as x_A is increased. However, the mode I energy release rate predicted by the FEA decreases rather slowly and remains almost constant when x_A ranges from 2 to 4 mm. Similar to the case at crack tip B, a reasonable agreement is observed only for joints with a relatively large half-crack length x_A. It is noted that the mode I energy release rate at crack tip A is larger than that at crack tip B. As shown in Fig. 11d, the FEA predicts that the mode II energy release rate at crack tip A increases with x_A. The analysis using the method in Ref. 15 predicts a decrease of mode II energy release rate with x_A, which is quite different from the FEA prediction. The analytical results using the method outlined in Ref. 16 indicate that the mode II energy release rate decreases when the half-crack length is between 1 and 2 mm and then increases when the half-crack length is longer than 2 mm. Once again, a reasonable correlation is observed only between the FEA and the analytical results of the Hutchinson and Sou[16] method for joints with a large x_A.

This observed poor correlation for joints with short cracks may be because it is not appropriate to model each cracked component near the crack tips using the classical beam theory. To capture variations of strain and stresses across the thickness of each cracked component, a higher-order beam theory should be used instead of the classical beam theory.

The mode I energy release rate at crack tip A is larger than that at crack tip B, whereas the mode II energy release rate at crack tip A is smaller than that at crack tip B. For the material system considered, the critical value of mode I energy release rate is much smaller than that of mode II energy release rate; thus, crack tip A tends to be more critical than crack tip B for the joint geometry considered. This may be regarded as one reason why crack propagation was experimentally observed at crack tip A.

Figure 12 shows the axial forces $P_1^{(B)}$ (see Fig. 10) predicted using the analytical model [Eq. (9)] and that calculated using FEA. Apparently, there is good agreement between the FEA results and the analytical predictions. Thus, it is clearly seen that the analytical model can predict the axial forces with good accuracy. These axial forces will be used to calculate the maximum stresses in the surface ply, which will then be compared to the tensile strength of an individual ply to predict the joint strength.

V. Correlation Between Experimental and Theoretical Results

As shown in the preceding section, the energy release rates at both crack tips and the axial forces in the cracked joints can be predicted using FEA and the analytical model. To predict failure loads for the specimens studied, the following two types of failure criteria will be incorporated in both FEA and analytical analysis.

1) Using the energy release rate criterion (ERC), it is assumed that a crack propagates when the following simple bilinear interaction criterion is satisfied[17]:

$$(G_{II}/G_{IIC}) + (G_I/G_{IC}) = 1$$

where G_{IC} and G_{IIC} are the critical energy release rates of modes I and II. The values for T300/934 plain weave cloth material were given in the preceding section.

2) Using the maximum stress criterion (MSC) for the surface ply, it is assumed that failure occurs when the average tensile stress in the surface ply attains its in-plane tensile strength.

Both failure criteria were used to predict the failure loads for the specimens in specimen groups A–F. Table 10 tabulates the average failure loads measured and the failure loads predicted using the FEA and the analytical methods. Crack initiation failure was predicted to occur at crack tip A based on the ERC. This is because crack tip A is more critical than crack tip B because it has a much higher failure index. Based on the MSC, sectional tensile failure was predicted to take place in the surface ply immediately outside the edge of the overlap. The failure loads predicted using the analytical model incorporating the methods in Refs. 15 and 16 and the energy release rate criterion are lower than the measured failure loads, as well as other predicted failure loads. This is because the energy release rates at crack tip A are overestimated using the analytical model. The failure loads predicted using FEA incorporating both criteria are in good agreement with the measured failure loads. In Table 10, there is very good agreement between the experimental results and the theoretical predictions (fifth column) given by the analytical model incorporating the maximum stress criterion for the surface ply. Figure 13 plots the failure loads measured and predicted vs the half-crack length. Among the predictions, the analytical model incorporating the maximum stress criterion gives the best correlation with the failure loads measured.

Sectional tensile fracture using both FEA and the analytical model is predicted to take place in the surface ply immediately outside the overlap. This is in good agreement with the observed sectional fracture in the surface ply, as discussed in the earlier experimental investigation section.

For specimen groups E and F, failure loads are predicted only using the FEA and the MSC for the surface ply. The predicted failure load for specimen group F correlates well with the measured one. This indicates that the cracks placed inside the overlap reduce the failure load in comparison with the virgin-type joint group. For specimen group E, unlike the experimental observation, a reduction in predicted failure load is noted. One possible reason for this is that sharp cracks are modeled in the FEA, whereas notches could have been created by inserting Teflon film in the specimen.

Table 10 Comparison between the average measured and the predicted failure loads, N

Specimen group	Average measured failure load	FEA (MSC)	FEA (ERC[13])	Theory (MSC)	Theory (ERC[15])	Theory (ERC[16])
A	14,171	13,944	——	13,594	——	——
B	12,598	12,074	12,670	12,079	7,435	5,265
C	13,004	12,096	12,375	12,602	8,628	7,583
D	13,395	12,168	12,433	12,984	9,853	11,860
E	14,020	12,487	——	——	——	——
F	13,263	12,086	——	——	——	——

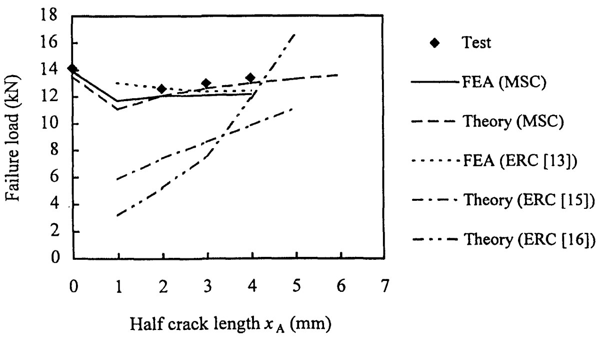

Fig. 13 Failure loads measured and predicted vs the half-crack length x_A.

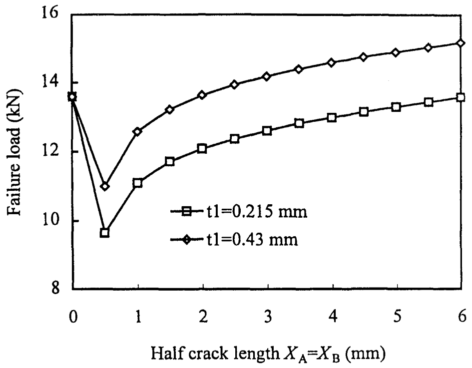

Fig. 14 Predicted failure loads vs the half-crack length.

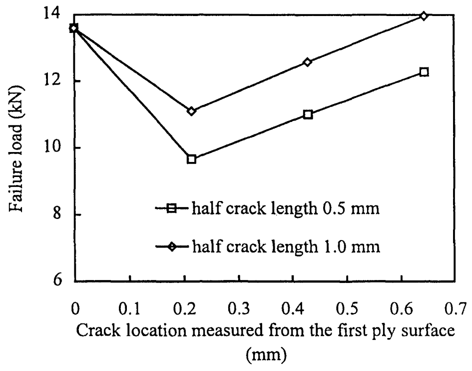

Fig. 15 Predicted failure loads vs the location of cracks at a distance measured from the first ply surface.

The analytical model and the MSC are then used to illustrate the effect of position of the crack on the failure loads. Figure 14 plots the predicted failure loads vs the half-crack length for two crack locations, i.e., $t_1 = 0.215$ and 0.43 mm. It is seen that a crack between the second and third plies ($t_1 = 0.43$ mm) tends to cause less load reduction than a crack between the first and second plies ($t_1 = 0.215$ mm). Figure 15 shows the predicted failure loads vs the crack location measured from the adherend surface for two half-crack lengths of 0.5 and 1.0 mm. A short crack close to the surface tends to be more detrimental in terms of reducing the failure load than a long and deep crack.

VI. Conclusions

An experimental and analytical study was carried out to investigate the effect of cracks embedded in continuous adherends near overlap ends on failure behavior of adhesive-bonded composite single lap joints. A simple analytical model was developed to predict the axial forces, transverse shear forces, and bending moments, as well as energy release rates of modes I and II in an adhesive-bonded cracked single lap joint. Good agreement was obtained between the average failure loads measured and those predicted using FEA and the present analytical model incorporating the MSC for surface ply. From the present results within the range of joint geometries tested and analyzed, the following is concluded. 1) When a crack has its center located right at an overlap end, it reduces the failure load. A short crack causes a larger reduction in failure load than a long crack. A crack between the first and second plies has a more detrimental effect on the joint strength than a crack of the same length between the second and third plies. 2) When a crack is located completely inside the overlap, it causes noticeable reduction in the failure load. 3) When a crack is placed completely outside the overlap of a joint, it may not affect the joint strength.

Appendix: Constants in Displacements

For simplicity, let us introduce the following notations:

$$\bar{c}_{20} = \frac{D_{2L}(\theta_A - \theta_B) - 0.5tx_A P_1^{(B)}}{D_{1L}x_A + D_{2L}x_B}$$

$$\bar{c}_{21} = -\frac{D_{1L}x_A^2 - D_{2L}x_B^2}{2(D_{1L}x_A + D_{2L}x_B)}, \qquad \bar{c}_{10} = \theta_B + x_B\bar{c}_{20}$$

$$\bar{c}_{11} = -0.5x_B^2 + \bar{c}_{21}x_B$$

$$\bar{c}_{30} = \bar{c}_{11}(x_A + x_B) + \frac{1}{2}\bar{c}_{21}\left(\frac{D_{1L}}{D_{2L}}x_A^2 - x_B^2\right) + \frac{1}{6}\left(\frac{D_{1L}}{D_{2L}}x_A^3 + x_B^3\right)$$

$$\bar{c}_{31} = w_A - w_B - \frac{tx_A^2 P_1^{(B)}}{4D_{2L}} - \bar{c}_{10}(x_A + x_B) - \frac{1}{2}\bar{c}_{20}\left(\frac{D_{1L}}{D_{2L}}x_A^2 - x_B^2\right)$$

where

$$w_B = w_1|_{x_1 = l - x_B}, \qquad w_A = w_2|_{x_2 = x_A}$$

$$\theta_B = \left.\frac{\mathrm{d}w_1}{\mathrm{d}x_1}\right|_{x_1 = l - x_B}, \qquad \theta_A = \left.\frac{\mathrm{d}w_2}{\mathrm{d}x_2}\right|_{x_2 = x_A}$$

and where θ_A and θ_B represent the slope of the deformed beam parts A and B, respectively.

Thus the eight constants in Eq. (14) are given by

$$c_3 = \bar{c}_{31}/\bar{c}_{30}, \qquad c_2 = \bar{c}_{20} + \bar{c}_{21}c_3, \qquad c_1 = \bar{c}_{10} + \bar{c}_{11}c_3$$

$$c_0 = w_B + c_1x_B - \tfrac{1}{2}c_2x_B^2 + \tfrac{1}{6}c_3x_B^3, \qquad c_4 = c_0$$

$$c_5 = c_1, \qquad c_6 = (D_{1L}/D_{2L})c_2 - (t/2D_{2L})P_1^{(B)}$$

$$c_7 = (D_{1L}/D_{2L})c_3$$

and D_{1L} as defined in the text.

Acknowledgments

The author is grateful to the grant awarded under the University of Sydney Research Grant Scheme. The author wishes to thank M. Bateup for his assistance in carrying out the tests.

References

[1] Adams, R. D., "Strength Predictions for Lap Joints, Especially with Composite Adherends. A Review," *Journal of Adhesion*, Vol. 30, 1989, pp. 219–242.

[2] Kairouz, K. C., and Matthews, F. L., "Strength and Failure Modes of Bonded Single Lap Joints Between Cross-Ply Adherends," *Composites*, Vol. 24, No. 6, 1993, pp. 475–484.

[3] Goland, M., and Reissner, E., "The Stresses in Cemented Joints," *Journal of Applied Mechanics*, Vol. 66, March 1944, pp. A17–A27.

[4] Hart-Smith, L. J., "Adhesive-Bonded Single Lap Joints," NASA CR-112236, Jan. 1973.

[5] Oplinger, D. W., "A Layered Beam Theory for Single Lap Joints," Army Materials Technology Lab., Rept. MTL TR91-23, 1991.

[6] Tsai, M. Y., and Morton, J., "An Evaluation of Analytical and Numerical Solutions to the Single-Lap Joints," *International Journal of Solids and Structures*, Vol. 31, No. 18, 1994, pp. 2537–2563.

[7] Tong, L., "Bond Strength for Adhesive-Bonded Single Lap Joints," *Acta Mechanica*, Vol. 117, Nos. 1–4, 1996, pp. 101–113.

[8] *ICI Fiberite Materials Handbook*, Tempe, AZ, March 1989.

[9] *Strand—Finite Element Analysis System*, G + D Computing, Sydney, Australia, Sept. 1996.

[10] *Boeing Advanced Composites Handbook*, The Boeing Co., Seattle, WA, 1986.

[11] Saghizaden, H., and Dharan, C. K. H., "Delamination Fracture Toughness of Graphite and Aramid Epoxy Composites," *Journal of Engineering Materials and Technology*, Vol. 108, Oct. 1986, pp. 290–295.

[12] Sheppard, A., Kelly, D., and Tong, L., "A Damage Zone Model for the Failure Analysis of Adhesively Bonded Joints," *International Journal of Adhesion and Adhesives* (to be published).

[13] Rybicki, E. F., and Kanninen, M. F., "A Finite Element Calculation of Stress Intensity Factors by a Modified Crack Closure Integral," *Engineering Fracture Mechanics*, Vol. 9, No. 4, 1977, pp. 931–938.

[14] Johnson, W. S., "Stress Analysis of the Cracked-Lap-Shear Specimen: An ASTM Round Robin," *Journal of Testing and Evaluation*, Vol. 15, No. 6, 1987, pp. 303–324.

[15] Williams, J. G., "On the Calculation of Energy Release Rates for Cracked Laminates," *International Journal of Fracture*, Vol. 36, No. 2, 1988, pp. 101–119.

[16] Hutchinson, J. W., and Suo, Z., "Mixed Mode Cracking in Layered Materials," *Advances in Applied Mechanics*, Vol. 29, 1992, pp. 63–191.

[17] Reeder, J. R., "A Bilinear Failure Criterion for Mixed-Mode Delamination," *Composite Materials: Testing and Design*, Vol. 11, ASTM STP 1206, American Society for Testing and Materials, Philadelphia, PA, 1993, pp. 303–322.

A. M. Waas
Associate Editor